On the 2D Post-Processing of Brillouin Optical Time-Domain Analysis

Simon Zaslawski 🆔, Zhisheng Yang 🆔, *Member, OSA*, and Luc Thévenaz 🆔, *Fellow, IEEE, Fellow, OSA*

Abstract—The benefits and limitations inherent to the 2D post-processing of measurements from Brillouin optical time-domain analyzers are investigated from a fundamental point of view. In a preliminary step, the impact of curve fitting on the precision of the estimated Brillouin frequency shift is analyzed, enabling a fair comparison between the representative noise-reduction algorithms studied in this article. The performances in terms of signal-to-noise ratio, experimental uncertainty σ_B on the Brillouin frequency shift and spatial resolution delivered by advanced image processing methods—such as wavelet transform and non-local means algorithms—are then compared with the impact of a 2D Gaussian filter. The major discrepancies observed when comparing the gain in signal-to-noise ratio to the σ_B reduction are then determined by exploiting the separability of the Gaussian filter, which reveals that noise reduction is only effective along 1-D of the 2D array of measurements and originates from a digital reduction of the system analog bandwidth. The signal-to-noise ratio improvement obtained from filtering in the spectral dimension is only illusory, since its action is redundant with the curve fitting procedure to estimate the Brillouin frequency shift. Finally, the maximum σ_B reduction achievable by digital post-processing is theoretically given, hence setting a fundamental limit to the improvement brought by data processing.

Index Terms—Brillouin scattering, optical fibers, signal processing, optical fiber measurement applications.

I. INTRODUCTION

BRILLOUIN scattering refers to the inelastic scattering of light over material compressive waves, i.e., acoustic vibrations, in the propagation medium [1], [2]. This effect can be optically stimulated through electrostriction (Stimulated Brillouin scattering or SBS) and has been widely exploited in optical fibers to achieve distributed measurements of both temperature and strain, a technique known as Brillouin optical time-domain analysis (BOTDA). In BOTDA, an optical pulse (pump) counter-propagating with a continuous-wave signal (probe) locally triggers SBS, leading to an energy transfer between pump and probe. This interaction shows a sharp resonance conditioned to a strict phase matching realized when the optical interference beating and the traveling acoustic wave are synchronous. Under this condition the frequency detuning between the two optical waves in presence matches the frequency of the acoustic wave involved in the scattering process, also known as Brillouin frequency shift (BFS). Quite remarkably, the BFS varies linearly with both temperature and strain in ambient conditions and a spatially-resolved temperature or strain profile over the whole length of the optical fiber can be obtained using BOTDA.

The first reports involving BOTDA for distributed temperature and strain sensing were published in 1990 [3], [4]. The technique has benefited since then from over three decades of continuous development. The development has been so extensive that standard BOTDA configurations are now facing physical limitations, such as the onset of modulation instability for the pump [5] and pump depletion for the probe [6]–[9], setting a hard limit to their power at fiber input. This in turns bounds the signal-to-noise ratio (SNR) on the response for a given spatial resolution at a certain distance as a simple consequence of fiber attenuation. These limitations have been yet partially circumvented by implementing sophistications such as distributed Raman amplification [10] or optical pulse coding [11]–[14], which have successfully proved to outperform the classical BOTDA configuration. More recently, the scientific community started to pay a substantial interest to noise removal techniques as used for image and video processing [15], since it was believed to raise at negligible cost the signal-to-noise ratio of the majority of existing setups, hence proportionally reducing the final measurement uncertainty [16]. Post-processing is an added layer in the system and can additively complement the previously cited sophistications.

In most BOTDA configurations, BFS evaluation is a two steps process: 1) the local Brillouin gain experienced by the probe is first measured along the optical fiber on a grid of equally spaced pump-probe frequency detuning values. 2) the gain curve associated to each position, referred to as Brillouin gain spectrum (BGS), is then processed in order to extract the corresponding BFS. This is commonly addressed using a fitting procedure, as the acquired data are inevitably corrupted by noise. The shape and full width at half-maximum (FWHM) of the Brillouin gain spectrum are dependent on the sensing fiber, the preset spatial resolution (SR) and the pump pulse shape [17]. At broad SR, that is 3 m and above corresponding to pulse widths equal or larger than 30 ns, the BGS matches a Lorentzian distribution whereas it turns closer to a Gaussian function when the SR is brought down to 1 m (10 ns pulse width). For such reasons, the most common BFS retrieval techniques consist in
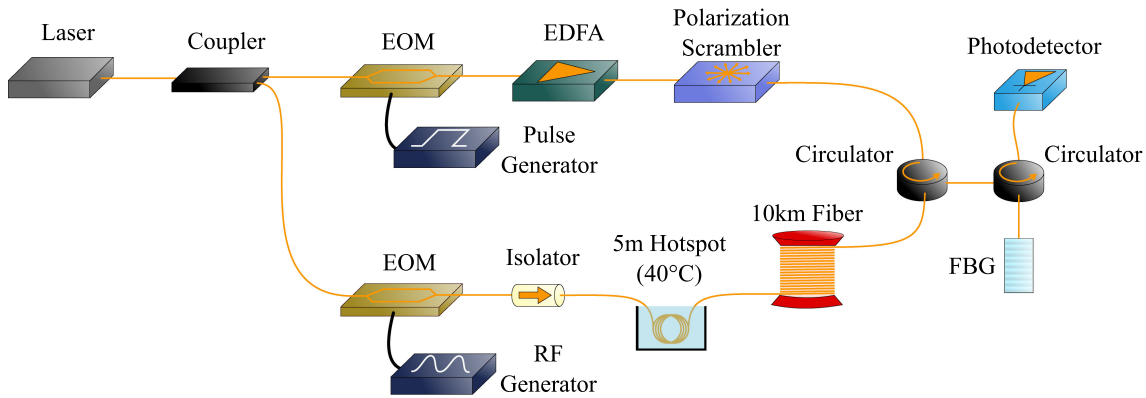
Fig. 1.   Experimental setup of the standard BOTDA sensor used for the different validations. EOM: electro-optic modulator, EDFA: erbium-doped fiber amplifier, RF: radio frequency, FBG: fiber Bragg grating.

either fitting a Lorentzian curve [18] over the whole BGS, or only keeping the upper part before performing a quadratic fitting [16]. More recently, a Lorentzian cross-correlation technique [19], [20] proved to be a promising alternative to the traditional fitting.

The first image processing techniques implemented for noise removal in BOTDA measurements were the orthogonal discrete wavelet transform (ODWT) and the non-local means (NLM) algorithms, providing SNR improvements of 13 dB [15]. However, it remains unclear whether such improvement will fully reflect on the BFS uncertainty reduction while perfectly preserving the original SR under any circumstance. Wu *et al.* reported more recently similar results using another sophisticated image processing algorithm called BM3D [21]. Interestingly, they also compare the distortion induced to the BFS distribution by the different methods for different SNR improvements. Although the general qualitative behavior of any noise removal technique is well understood, in the sense of a tradeoff between noise removal and signal distortion, to the best of our knowledge a fundamental explanation is still missing to evaluate the SNR improvement resulting from a given method and under what condition the implemented algorithm will maintain the instrumental SR.

In this paper, we aim at clarifying the intricate relationships linking signal-to-noise ratio, measurement uncertainty and BFS distribution, while evaluating the impact of post-processing on these quantities. First, we demonstrate the importance of carefully optimising the procedure to estimate the BFS from the measurements [22]; if not, the real SNR improvement may turn out to be misevaluated by data post-processing. We then challenge the observed SNR improvement after processing experimental BOTDA measurements using either the ODWT or NLM with the corresponding reduction in BFS uncertainty σ_B. Quite counterintuitively, we observe major discrepancies between SNR improvement and σ_B reduction, since a given SNR improvement does not correspond to an identical uncertainty reduction, as would be expected [16]. Although the SNR improvement exceeds 10 dB for most techniques, σ_B could only be reduced by a factor 3 without influencing the sensor SR. This was later explained by comparing the results obtained using a separable 2D Gaussian filter [22]. It turns out that noise removal

is only effective when applied to the time-domain Brillouin gain traces, as the fitting procedure applied to each BGS already filters out noise, thus making the use of another filter or noise removal algorithm redundant. The observed noise reduction was attributed to the numerical reduction of our photodetector bandwidth, which is broader than our signal bandwidth and thus collects the extra noise out of the signal bandwidth.

II. EXPERIMENTAL SETUP

Measurements were acquired at 1 m, 2 m and 5 m spatial resolution based on the standard BOTDA setup depicted in Fig. 1. The light from a laser operating at 1550 nm is split in two branches using an optical coupler. A high extinction ratio electro-optic modulator (EOM) is inserted in the upper branch to shape the continuous-wave (CW) signal from the laser into a pulse that is then amplified by an erbium-doped fiber amplifier (EDFA) before being launched into the sensing fiber through an optical circulator. The lower branch contains a second EOM operating in double sideband carrier-suppressed mode and driven by a tunable frequency RF signal to generate a probe signal with proper frequency detuning with respect to the pump. After its propagation through the sensing fiber, the probe sees one of its sidebands filtered out by a fiber Bragg grating before detection. The polarization-induced fading effects are mitigated by use of a polarization scrambler on the pump branch. Finally, the isolator prevents the strong residual pump pulse from further circulating in the setup.

Though the sensing fiber is kept short (10 km), the pump and probe powers were always maintained below 23 dBm [5] and −6 dBm [6]–[9], respectively, in order to secure the absence of spurious effects such as modulation instability and pump depletion. The pump power was then finely tuned for each SR in order to obtain a 3 dB SNR at the fiber distant end using 16 averages. Given the square root dependence of SNR on the number of averages, the measurements were repeated by quadrupling the averaging number in order to reach 6 dB (64 averages) and 9 dB (256 averages) SNR at the fiber distant end. In addition, a reference profile was acquired at 12 dB SNR at the fiber distant end (1024 averages) for every SR. Finally, ~5 m of

the sensing fiber were placed in a thermal stabilized bath at 40 °C to create a hot spot to evaluate the sensor spatial resolution for different post-processing approaches.

III. BRILLOUIN FREQUENCY SHIFT RETRIEVAL

Essentially BOTDA sensors aim at determining the Brillouin frequency shift (BFS) of an optical fiber over its entire length. This is generally realized by spectrally sampling the Brillouin gain spectrum (BGS) before extracting the central frequency. The problem of accurately and precisely determining the BFS from a noisy BGS has been studied from the early stages of BOTDA sensors development and is still a hot topic today [16], [18], [19], [22]. It has been recently thoroughly addressed by Haneef *et al.* [20] and will thus not be deeply analyzed here. A succinct evaluation of the performances achieved by quadratic fitting using various parameters is therefore carried out. This preliminary step is crucial to figure out and fully evaluate the real benefits from noise reduction algorithms, considering that quadratic fitting is also applied to denoised data.

As mentioned in the introduction, the BGS spectral distribution depends on the tested fiber, the preset spatial resolution and the waveform of the pump pulse. In our case, the use of an electro-optic modulator (EOM) driven by a 600 MHz pulse generator produced quasi-rectangular pump pulses. At 5 m SR and above, corresponding to ≥50 ns pump pulses, the BGS measured is very similar to the natural Lorentzian Brillouin lineshape. Decreasing the SR down to 2 m (20 ns) did not significantly alter the BGS distribution, but already resulted in a noticeable broadening. Bringing the sensor SR down to 1 m (10 ns) modified the BGS even more, making its distribution closer to a Gaussian curve than a Lorentzian. For a fair comparison, the same fitting procedure was applied at all SR. In this paper, BFS estimation was realized by fitting a second order polynomial to the upper part of the BGS around the peak value. As emphasized in [20], quadratic fitting requires a prior estimate of the BFS location to deliver accurate results. This was carried out by sweeping a moving average filter with $N = 31$ samples and identify the maximum of the smoothed BGS. The complete fitting procedure is illustrated in Fig. 2.

The precision of any BOTDA sensor is ultimately defined by the uncertainty of the measured BFS σ_B. For a quadratic fitting procedure, σ_B is inversely proportional to the SNR, and under optimized conditions the following expression is given [16]

$$\sigma_B = \frac{1}{\text{SNR}} \sqrt{\frac{3\delta\Delta\nu_B}{8\sqrt{2}(1-\eta)^{3/2}}} \tag{1}$$

where δ is the frequency detuning scanning step, $\Delta\nu_B$ is the BGS FWHM and η is a threshold level defining the subset of data points relevant for the fitting. For a normalized gain curve, for which values range from 0 to 1, the quadratic fitting is restricted to points greater than η. As intuitively anticipated, raising the number of points over which the quadratic fitting is performed by decreasing η is expected to lower σ_B. This behavior was experimentally verified by acquiring 10 repeated BOTDA measurements, retrieving the BFS using a quadratic fit for a range of fitting window sizes W_{fit} and finally computing the
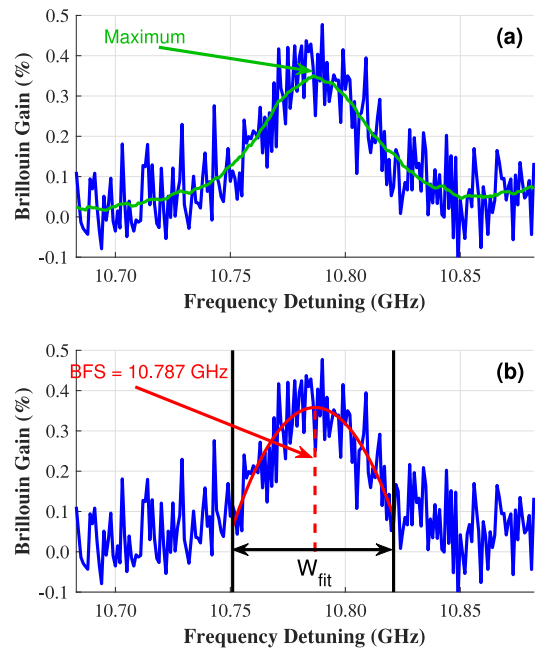

Fig. 2. Fitting procedure over a BGS measured at 6 dB SNR with 2 m spatial resolution. After a prior coarse estimation of the BFS using a moving average filter (a), a quadratic curve is fitted over a reduced set of points around this initial value to estimate the final BFS (b).
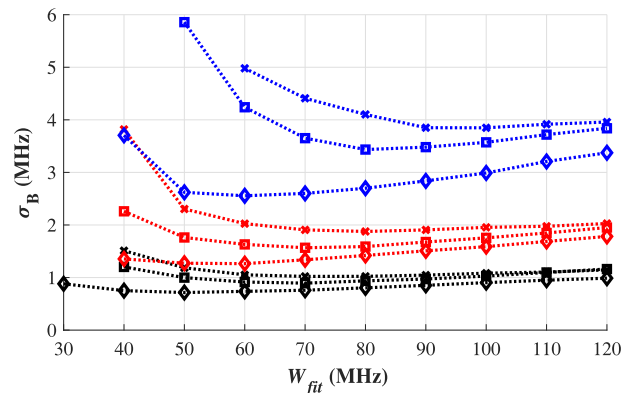

Fig. 3. BFS standard deviation σ_B computed over 10 repeated BOTDA measurements for three different SNR levels (color) and at three spatial resolutions (ticks). SNR: 3 dB (blue), 6 dB (red) and 9 dB (black). Spatial resolution: 1 m ($\cdots \times \cdots$), 2 m ($\cdots \square \cdots$) and 5 m ($\cdots \Diamond \cdots$).

corresponding standard deviation σ_B. The results are presented in Fig. 3.

The results illustrate the need for a sufficiently wide fitting window when estimating the BFS using a quadratic fitting and, it turns out to be quite critical at low SNR (blue curves). For instance, at 2 m SR, the BGS FWHM is approximatively equal to 50 MHz. However, the improper choice of the window size to this FWHM results in an uncertainty almost twice larger than for a properly sized window, that is 80 MHz when the SNR is equal to 3 dB (blue, squares). This is important to get results that are more precise and it turns crucial for the comparison between noise removal techniques, since the benefit brought by an algorithm may be significantly overestimated. To illustrate this feature, let consider a denoising method rising the SNR

level from 3 dB to 6 dB at 2 m SR, i.e., moving from the blue curve with square symbols to the red curve with square symbols. For W_{fit} equal to 50 MHz, the apparent uncertainty reduction is almost 4 MHz (from 5.9 MHz to 1.8 MHz) while it is slightly below 2 MHz (from 3.4 MHz to 1.6 MHz) for the proper window size of 80 MHz. Note that in the first case, SNR improvement (a factor 2) and uncertainty reduction (almost a factor 3) are not consistent. By contrast a full consistency is observed for the proper 80 MHz window (factor 2 on SNR and σ_B).

IV. NOISE REMOVAL IN BOTDA MEASUREMENTS

From a signal processing point of view, daily-life images contain by essence many abrupt transitions, for example due to the presence of diverse objects or due to regions presenting complex textures. Using low-pass filters straightforwardly on a noisy image will inevitably cause a blurring effect due to the smoothing of the many edges present in most images. Advanced non-linear algorithms such as NLM or the ODWT raised considerable interest in the scientific community because they enable to more accurately collect the information contained in an image from a visual point of view [23], [24]. A BOTDA measurement is a 2D matrix containing the values of the Brillouin gain at each position for each frequency detuning step. By convention, we designate the measure of the Brillouin gain versus distance at a given frequency detuning as the Brillouin gain profile (BGP), in contrast to the Brillouin gain spectrum (BGS) corresponding to the values of the Brillouin gain at a given position as a function of frequency detuning. As such, its structure does not differ fundamentally from a grayscale image, for which a value is associated to each pixel. This stemmed the use of the aforementioned image-processing techniques for noise removal in BOTDA measurements, taking advantage of the significant research dedicated to this field. The ODWT and NLM immediately showed a great potential for noise removal in BOTDA measurements, as improvements in SNR greater than 10 dB were reported [15].

Although BOTDA matrices may be processed as images, they are yet radically different from most daily life images. BOTDA measurements are actually very smooth and uniform when compared to the different contents found in any image, and thus their spectral content is expected to be essentially located at low frequencies. Following this approach, we challenged the results obtained using NLM and the ODWT with those using a 2D Gaussian filter. Gaussian filters show several remarkable features, such as excellent time-frequency confinement as well as a straightforward design depending on a single parameter. Gaussian filters were initially proposed by Le Floch *et al.* [25], demonstrating a simple and effective approach to enhance the performances of BOTDR setups. The filter tuning procedure here employed is similar, yet complementary by exploiting the separability of Gaussian filters to dissociate and analyze the contribution from each dimension to the total filtering operation.

This section is devoted to the thorough analysis of the impact brought by 2D noise removal on SNR, BFS uncertainty (σ_B) as well as effective spatial resolution (SR). SNR improvements similar to those previously reported in the literature have been
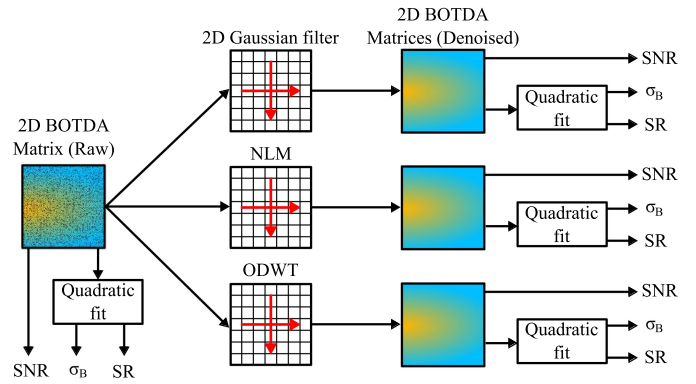

Fig. 4. Block diagram illustrating the comparison procedure employed to evaluate the benefit brought by 2D noise reduction in BOTDA. The quadratic fit was optimized before and after noise removal following the conclusions drawn in Section III.

observed, regardless of the 2D method used. However, such improvements did not result in a similar decrease in σ_B, as might have been expected (1). This apparent discrepancy can be explained when splitting the 2D Gaussian filtering into two 1D contributions. It turned out that noise removal is only effective in one dimension, corresponding to the filtering of each acquired BGP. This can be explained by observing that the bandwidth of the photodetector - 125 MHz in our case - is broader than the signal bandwidth, itself intrinsically related to the pulse width. The benefit of filtering is thus to suppress the noise generated by the photoreceiver at higher frequencies. Filtering of each BGS in the other dimension is actually redundant with the fitting operation and thus does not impact on the accuracy in the BFS determination.

A. SNR Improvement and σ_B Reduction Using 2D Processing Techniques.

This section addresses the influence of different 2D noise removal on SNR, BFS uncertainty (σ_B) reduction and spatial resolution impairement as illustrated in Fig. 4. The methods under evaluation are the NLM, the ODWT as well as 2D Gaussian filtering. The procedure used to adjust the 2D Gaussian filter is detailed hereafter. The parameters used for NLM and the ODWT are mostly based on a previously published work [15]. A succinct description of the operating principle for the Gaussian filter, NLM as well as the ODWT can be found in Appendix A.

Taking advantage of the separability of the 2D Gaussian filter, the two standard deviations (σ_{BGP}) and (σ_{BGS}) governing the coverage of the filter in either dimension are set independently. In BOTDA, these parameters depend almost exclusively on the experimental SR. On one hand, the pulse width limits the sharpness of the transitions observed in a given BGP. On the other hand, the spatial resolution also shapes the measured BGS, as its distribution results from the convolution between the fiber fundamental Brillouin linewidth and the pulse spectrum [17].

$$\sigma_{\text{BGP}} = \frac{W_{\text{pulse}}}{k_{\text{BGP}}} \quad , \quad \sigma_{\text{BGS}} = \frac{\text{FWHM}}{k_{\text{BGS}}} \qquad (2)$$

TABLE I
SNR AND BFS UNCERTAINTY COMPARISON

	SNR [dB] / σ_B [MHz]		
Raw data	3.1 / 3.49	6.2 / 1.70	9.3 / 0.94
2D Filter	13.9 / 1.23	17.1 / 0.53	20.0 / 0.34
NLM	12.5 / 1.13	15.7 / 0.49	18.8 / 0.31
ODWT	12.5 / 1.15	15.7 / 0.55	18.7 / 0.37

The SNR (in dB) and BFS uncertainty (in MHz) were computed by averaging 200 samples at the fiber end.

Here W_{pulse} and FWHM are the pulse width in seconds and the BGS full width at half-maximum in Hz, respectively. The parameters k_{BGP} and k_{BGS} were introduced to provide some flexibility in the filter tuning. It turns out that, even for a fiber presenting a perfectly uniform BFS, neither the BGP nor the BGS are expected to be Gaussian, such that a bandwidth adjustment is mandatory. As will be detailed in Section IV-B, the choice of k_{BGP} is very critical and a too low value results in a spatial resolution impairment, while k_{BGS} is somehow less challenging, yet may lead to a bias in the determination of the BFS. A procedure to properly set k_{BGP} and k_{BGS} is provided in Section IV-C. The parameters assigned to the different methods are given here below:

- Experimental setup: The spatial resolution is 2 m (20 ns pulse width) for a sampling interval of 0.5 m (5 ns) and a detector bandwidth of 125 MHz. The frequency detuning scanning step was set to 1 MHz
- 2D Gaussian filter: Following (2), we use $k_{\text{BGP}} = 2$ and $k_{\text{BGS}} = 6$. The FWHM is evaluated to be approximatively 50 MHz.
- NLM: The search and similarity windows are adjusted to 13×13 and 3×3 samples, respectively. The parameter controlling the decay of the exponential response h is set to $5\sigma_n$, where σ_n is the white noise standard deviation estimated using the details coefficients resulting from the wavelet decomposition (see Appendix A–C for details).
- ODWT: The used mother wavelet is the symlet 7. The threshold is set to $0.5T_u$ where T_u is the universal threshold (see Appendix A–C), using a hard-thresholding approach.

Note that we conduct this study at 2 m spatial resolution, although similar conclusions may be reached at 1 m and 5 m spatial resolution. The SNR and σ_B evaluated at the end of our 10 km fiber before and after post-processing are reported in Table I. As expected, we observe major SNR improvements regardless of the used algorithm. All three techniques show similar SNR improvements, although 2D Gaussian filtering seems slightly more efficient in addition to preserving the instrumental spatial resolution, as confirmed by Fig. 5. However, these results are no longer consistent with equation (1). Overall, the SNR is increased by 10 dB which should in turn decrease σ_B by a factor 10, whereas the effective BFS uncertainty is roughly reduced by a factor 3. The 2D Gaussian filter moreover provides the highest SNR enhancement but does not lead to the lowest measured BFS uncertainty. The reasons behind such discrepancies are clarified in the following section.
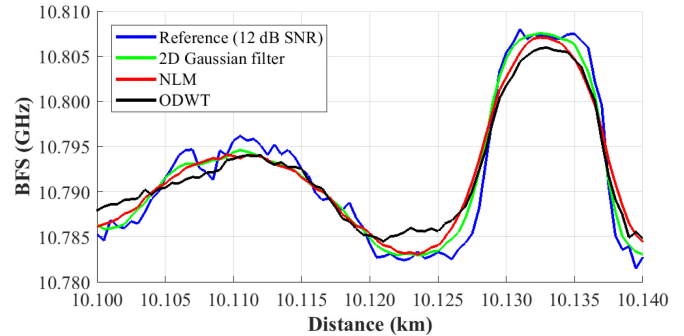

Fig. 5. BFS profile measured at hotspot for a spatial resolution of 2 m and an initial SNR of 3 dB before and after data post-processing.
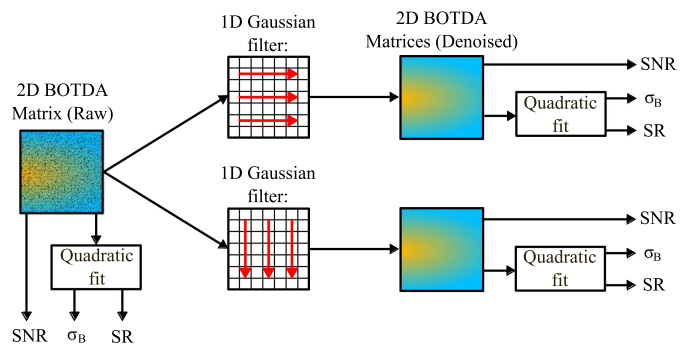

Fig. 6. Block diagram illustrating the comparison procedure employed to evaluate the benefit brought by 1D noise reduction using the Gaussian filters in BOTDA. The quadratic fit was optimized before and after noise removal following the conclusions drawn in Section III.

B. Origin of Noise Removal in BOTDA Measurements

The fundamental reasons leading to a reduced experimental uncertainty in BOTDA using digital post-processing are investigated. We take once more advantage of the separability of the 2D Gaussian filter to analyze in greater details its influence on either dimension of the BOTDA matrix. Again, any improvement in signal-to-noise ratio is compared to the corresponding reduction in BFS uncertainty, while simultaneously evaluating the preservation of the original spatial resolution. Note that the original data (raw) used here are the same as in the previous section. We apply a 1D Gaussian filter on each BGS or on each BGP, as illustrated in Fig. 6. The spread, and thus the strength of each filter is adapted by varying k_{BGP} between 1 and 3, and k_{BGS} between 2 and 6 in (2). Fig. 7 depicts the BFS profile obtained at the hotspot location, together with the corresponding SNR and σ_B.

The two considered cases considered show radically different behaviors. In the first situation (a), application of a Gaussian filter leads to a significant SNR improvement varying between 7 dB and 8 dB. However, there is almost no difference in experimental uncertainty as evidenced by the value taken by σ_B when k_{BGS} is equal to either 4 or 6. When k_{BGS} is too small, contradictory results apparently show up, in a sense that a greater SNR improvement (when compared to $k_{\text{BGS}} = 4, 6$)
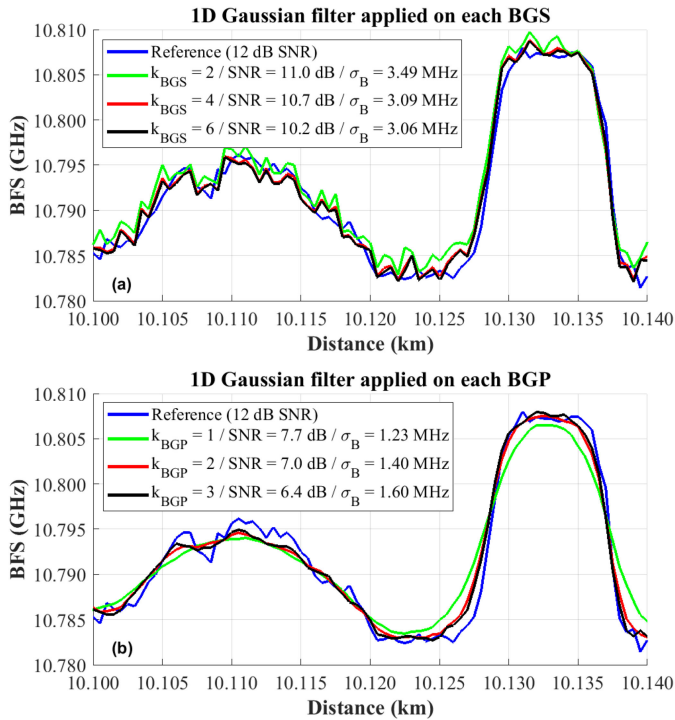
Fig. 7. BFS profile measured at hotspot for a spatial resolution of 2 m and an initial SNR of 3 dB after 1D Gaussian filtering. The filter is applied either on each BGS (a) or each BGP (b) for various filter strengths.

results in a poorer uncertainty. In addition, there is a noticeable bias in the obtained BFS. This is analyzed in more detail in Section IV-C, where we show that these observations stem from excessive filtering, i.e., that is the applied filter distorts the signal in addition to suppressing the noise. Furthermore, it must be highlighted how the BFS profiles measured are rigorously identical for $k_{BGS} = \{4, 6\}$, rising the suspicion that the filter plays no role in the determination of the BFS. This can be better understood when considering the action performed by the fitting procedure. Fitting a curve to a noisy data set corresponds to searching the slowly-varying function that will best approximate its general trend, since the sequence experiences rapid variations due to noise. Alternatively, it can also be considered as the extraction of the underlying low-pass information from a high-frequency signal. Polynomial fitting is actually equivalent to low-pass filtering using Savitzky-Golay filters [26]. To our understanding, the use of a Gaussian filter on each BGS is redundant with any BFS retrieval method as they all come down to a low-frequency information extraction. For instance, BFS retrieval by cross-correlation with a perfect Lorentzian curve is completely equivalent to the application of a Lorentzian-shaped low-pass filter, as cross-correlation and convolution provide, in this case, an identical output. Bearing these considerations in mind, digital filtering can provide alternate ways of evaluating the fiber BFS. In particular, efficient filtering operations via fast Fourier transform implementation can deliver remarkably rapid BFS estimations compared e.g., to fitting using iterative algorithm [20]. Finally, it must be pointed out that the use of a Gaussian filter keep slightly reducing the measurement

uncertainty, i.e., from about 3.5 MHz for raw data to approximatively 3.1 MHz after filtering. This is certainly due to quadratic fitting being not the optimum method for BFS retrieval, as the BGS distribution is not purely quadratic, and thus the use of a Gaussian filter provides a marginal improvement.

We will now consider the application of a 1D Gaussian filter on each BGP. Unlike the previous case, very distinct behaviors in terms of σ_B and BFS profile can be observed when varying k_{BGP} from 1 to 3, as depicted in Fig. 7(b). First, SNR and σ_B are now again consistent with (1), as verified by comparing the values obtained with those given in Table I for raw data. Actually, the SNR improvement for $k_{BGP} = \{1, 2, 3\}$ is equal to 4.6 dB (factor 2.88), 3.9 dB (factor 2.46) and 3.4 dB (factor 2.19), respectively. Dividing the BFS uncertainty for unprocessed data ($\sigma_B = 3.49$ MHz) by the corresponding factor leads to theoretical values of 1.21 MHz, 1.42 MHz and 1.59 MHz when $k_{BGP} = \{1, 2, 3\}$, respectively, in excellent agreement with the measured uncertainty provided in Fig. 7.(b) (1.23 MHz, 1.40 MHz and 1.60 MHz). Besides, the filter significantly smoothes the BFS profile when its strength increases, that is as k_{BGP} reduces. The impairment on the original spatial resolution is accompanied by a decrease in σ_B, evidencing an inevitable trade-off when using low-pass filters. We interpret the action of this 1D filter as a digital reduction of the photodetector original bandwidth. As commonly observed in BOTDA implementations, the detection bandwidth is broader than the signal bandwidth, making the system receptive to noise sources at frequencies containing no signal information. A low-pass digital filter with proper cutoff frequency will successfully suppress the noise originating from this portion of the electrical spectrum, thus reducing the experimental uncertainty without impairing the spatial resolution, whereas a stronger filter will start impinging on the signal spectrum. Finally, attention must be paid to the cumulated improvement brought by the individual filters for $k_{BGS} = 6$ and $k_{BGP} = 2$, which are equal to 7.1 dB and 3.9 dB, respectively, in excellent agreement with the 10.8 dB SNR improvement measured using a 2D Gaussian filter with identical parameters (see Table I), proving the separable action of this filter.

These observations are further illustrated by observing the fiber BGS after filtering with either 1D Gaussian filter. This is shown in Fig. 8 for an initial SNR of ~6 dB. For the sake of clarity, we remind here that noise reduction using a linear filter is carried out by performing a weighted average over the samples surrounding a given point. For Gaussian filters, the weights follow a Gaussian distribution and the corresponding kernel has a finite size. This way, a given data point is only influenced by neighboring points, which may induce smoothing, should the filter coefficients be too strong. This is clearly visible for the BGS filtered data (Fig. 8), which appears extremely smooth when compared to raw data. However, this improvement is only apparent since, as explained above, the fitting procedure performs a similar action. In addition, the use of a strong BGS filtering may lead to a bias in the BFS determination due to smoothing, should the BGS present additional side lobes originating from secondary acoustic modes or as a result of BFS non-uniformity over the spatial resolution. This effect is visible from Fig. 7(a) when $k_{BGS} = 2$ as a 1 MHz upwards shift of the estimated BFS
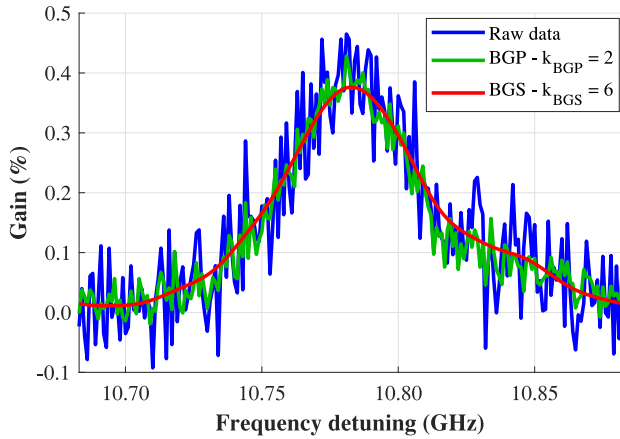
Fig. 8. BGS at 2 m SR and 6 dB SNR before and after filtering with a 1D Gaussian filter applied on either dimensions of the BOTDA matrix.
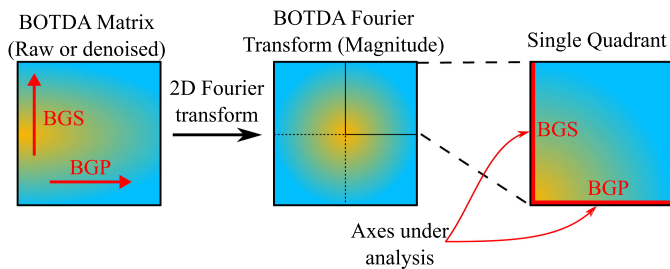

Fig. 9. Frequency analysis of BOTDA measurements using 2D discrete Fourier transform. The red lines indicate the axes over which this analysis is carried out (see Fig. 10 and Fig. 12).

Fig. 10. Magnitude of the 2D Fourier transform along the BGP axis: (a) Comparison between raw data (3 dB SNR) and reference (12 dB SNR), together with the Fourier transform of a Gaussian filter with $k_{BGP} = 1, 2$. The vertical lines indicate the cutoff frequency. (b) The same normalized Fourier transform before and after post-processing using a 2D Gaussian filter, NLM or the ODWT.

resulting from the influence of the additional acoustic mode seen on the upper frequency side of the main lobe in Fig. 8. The use of a BGP filtering results in clear noise reduction, without apparent distortion on the raw BGS. Yet, and since the Gaussian kernel mixes information from neighboring samples, a strong BGS filtering may lead to SR loss, as shown in Fig. 7(b).

C. Spectral Composition of BOTDA Measurements

Our arguments can be further proved by computing the 2D Fourier transform of BOTDA measurements and analyzing their spectral content. Since BOTDA measurements are real-valued signals, their Fourier transform is symmetric, such that we may only focus on a single quadrant as illustrated in Fig. 9. We then observe the 2D spectrum along two axes, indicated by red lines in Fig. 9, corresponding to Figs. 10 and 12. It turns out that BOTDA matrices are essentially low-frequency signals, suggesting why advanced filtering techniques are not performing significantly better than a low-pass filter.

1) Spectral Composition in BGP Direction: Fig. 10 depicts the magnitude of the 2D Fourier transform evaluated along the BGP axis. In other words, these spectra correspond to the frequency content of the 2D BOTDA matrix in the direction of the BGP. Fig. 10(a) illustrates the effect of averaging on SNR, which results in a change of the noise level. This way, part of the signal eventually merges in noise at low SNR (blue curve). Notice how
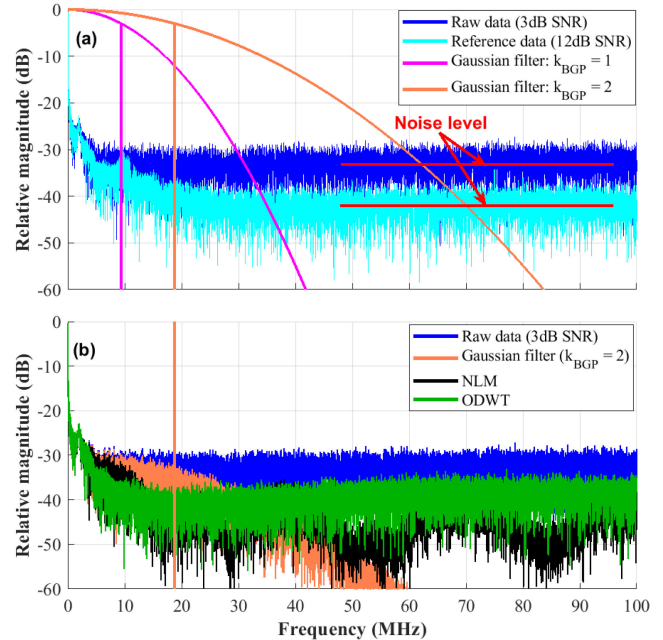
the fine details observable at 12 dB SNR (cyan curve) between 5 and 20 MHz eventually lie below the noise floor for a SNR of only 3 dB (blue curve). This enables to clarify two important points: 1) it explains why a Gaussian filter with $k_{BGP} = 1$ results in SR impairment (see Fig. 7), since its cutoff frequency is still within the signal bandwidth. 2) a most important aspect is that post-processing will never be able to compensate for a poorer initial signal-to-noise ratio, as the noise within the signal bandwidth cannot be eliminated without information loss. We place a strong emphasis on this aspect, as this defines a limit for noise removal in BOTDA measurements using post-processing. The maximum improvement that post-processing can achieve is to relegate the noise outside the signal bandwidth to negligible levels.

Fig. 10(b) depicts the frequency content of BOTDA matrices in BGP direction before and after post-processing. All techniques perform well outside the signal bandwidth, reducing the noise well below its original level. However, it appears that NLM and the ODWT are also reducing energy within the signal bandwidth, which should logically lead to worse SR. Although, this is not dramatically evidenced when observing the BFS at a transition (see Fig. 5), such a an impairment is much more sever in regions where the BFS less varies, as shown in Fig. 11. It clearly appears that although all techniques worsen the original SR, NLM and especially the ODWT induce a stronger smoothing. The two main reasons for this are: 1) Unlike filtering, NLM and the ODWT are local techniques, meaning that noise removal is not uniform over the whole BOTDA matrix, so that
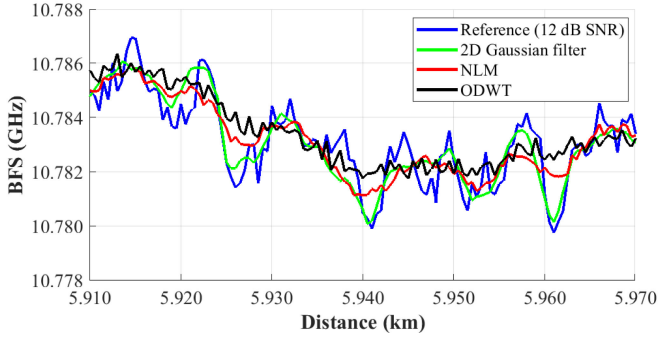
Fig. 11. BFS profile measured with a spatial resolution of 2 m and an initial SNR of 3 dB before and after data post-processing over a region where the BFS experiences moderate variations.
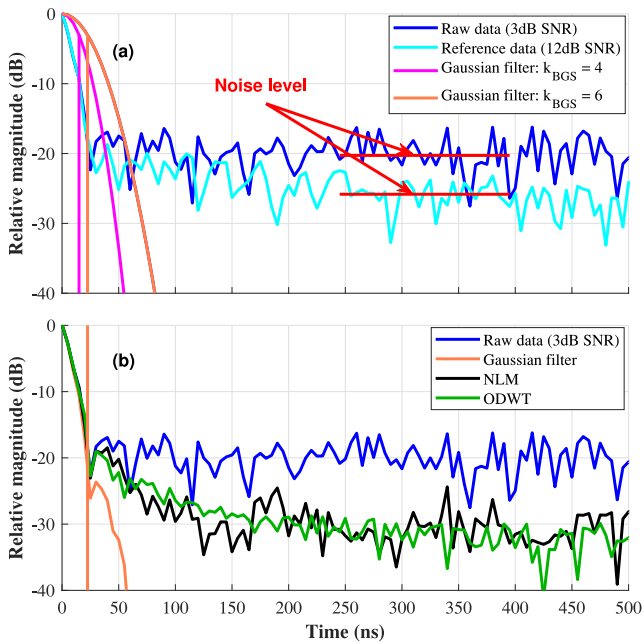

Fig. 12. Magnitude of the 2D Fourier transform along the BGS axis: (a) Comparison between raw data (3 dB SNR) and reference (12 dB SNR), together with the Fourier transform of a Gaussian filter with $k_{BGS} = 4, 6$. The vertical lines indicate the cutoff frequency. (b) The same normalized Fourier transform before and after post-processing using a 2D Gaussian filter, NLM or the ODWT.

regions containing abrupt transitions may be better maintained than uniform ones. 2) Eventually, and as detailed in Section IV-E, NLM and the ODWT turn out to perform like a low-pass filter, which in the particular case of BOTDA measurements is less adapted than the 2D Gaussian filter we designed.

2) Spectral Composition in BGS Direction: We analyze in turn the frequency content of BOTDA measurements in BGS direction, as depicted in Fig. 12. Note that the x-axis in Fig. 12 is time, because the original data has the unit of frequency (Hz). Again, Fig. 12(a) illustrates the detrimental rising of the noise floor for reduced averaging. The confinement of the signal energy in the low-frequency region is even stronger than for the other dimension (see Fig. 10(a)). As detailed in Section IV-D3,
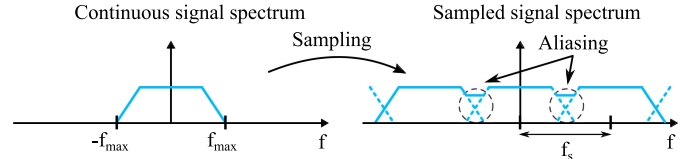

Fig. 13. Illustration of aliasing originating from the under sampling of a signal with maximum frequency $f_{max} > f_s/2$. Sampling creates replicas of the original continuous signal spectrum, spaced in the frequency domain by f_s. In order to avoid aliasing, one should ensure a sampling frequency $f_s \geq 2f_{max}$.

this explains why a 1D Gaussian filter applied over each BGS produces a significantly higher SNR improvement than a 1D Gaussian filter applied on each BGP (compare Fig. 7(a) and (b)). Actually, the larger the fractional bandwidth exclusively covered by noise, the more efficient is the noise removal. This figure also illustrates why setting k_{BGS} to 4 or lower may lead to a bias in the BFS determination, as the filter cutoff frequency (vertical lines) will lie within the signal bandwidth, thus leading to distortion. As explained in Section IV-B, any BFS retrieval method will only make use of the information contained within the low-frequency region and discard the rest, making the prior use of a low-pass filter redundant. In addition, the major inconsistencies observed when comparing SNR improvement to σ_B reduction after 1D filtering of each BGS (see Fig. 7) can be explained by the fact that (1) was derived assuming statistical independence between the samples constituting the gain spectrum. Although this remains valid when filtering each BGP independently, any method that operates transversally or in both dimensions will inevitably lead to correlating multiple points within the considered BGS, as all techniques employ a finite-size kernel to achieve noise reduction.

D. Noise Removal Efficiency Using Gaussian Filtering

To the best of our knowledge, no study aiming at anticipating the SNR improvement brought by a given noise reduction algorithm for BOTDA measurements has been conducted yet, such that this benefit could only be measured by comparing the initial SNR with the SNR reached after post-processing. In this section, we address this issue and illustrate how to evaluate the SNR enhancement brought by a Gaussian filter. We first recall some important concepts related to signal processing, as they are fundamental in understanding what kind of benefit digital filtering can provide.

1) Sampling and Aliasing: Practically, the optical system employed to perform BOTDA measurements is analog up to the photodetector output, which delivers a continuous-time signal proportional to the detected optical intensity. This signal is latter sampled using for instance an acquisition card and stored in a computer to further process it. According to the sampling theorem, a bandlimited signal may be perfectly reconstructed from its samples, provided that the sampling frequency f_s is at least twice greater than the signal's maximum frequency. In other words, a given sampling frequency enables reconstructing without errors signals which do not extend further than $f_s/2$. A violation of the sampling theorem leads to a folding of the energy lying above $f_s/2$ back into the measurable frequency range, as illustrated in Fig. 13, a phenomenon also known as aliasing.
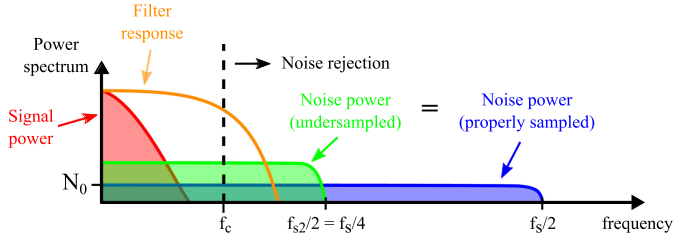
Fig. 14. Importance of proper sampling for efficient noise removal using digital filtering. In any case, the filter cutoff frequency f_c should be greater than the signal bandwidth, such that the latter does not get distorted by the filtering operation. In case of undersampling (f_{s2}), noise aliasing makes it impossible to reduce noise as much as when using a proper sampling rate f_s.

When considering deterministic signals, aliasing may lead to signal distortion. Undersampling makes impossible an accurate reconstruction of the original continuous-time signal, as some high frequency information turns mixed with lower frequency contents. Aliasing also occurs for random processes, i.e., noise, however with a frequency folding to be performed over the power spectral density [27]. Both types of aliasing may have detrimental effects for BOTDA measurements and should be strictly avoided in a proper design. In the following of this section, we shall consider that the sampling rate is significantly higher than the signal bandwidth while being lower than the noise bandwidth.

2) Signal-To-Noise Ratio (SNR) and Filtering: Fundamentally, signal-to-noise ratio is defined as the ratio between signal power and noise power. As explained in Section IV-C, proper noise removal is achieved by digital filtering provided that the signal remains unaffected by the filtering operation. This can only be made optimal if the sampling frequency is at least twice higher than the photodetector bandwidth, as illustrated in Fig. 14. Additive white Gaussian noise (AWGN) aliasing occurs when the noise intrinsic bandwidth exceeds $f_s/2$, which defines the observable frequency range upper bound. Fig. 14 depicts both cases of proper (blue) and insufficient (green) sampling rate. AWGN has constant power spectral density N_0 over the captured frequency range. In this example, halving the sampling frequency results in reducing the measurable frequency range by two, leading to severe noise aliasing. As a consequence, a higher noise level is now observed over a reduced frequency range. Note that although AWGN aliasing leads to an increase in noise level [28], the integrated noise power remains the same, because aliasing of random processes leads to a summation in terms of power spectral density [27]. If no digital filter is applied, the measured signal-to-noise ratio will remain identical, independently of the sampling frequency. The importance of proper sampling lies in the potential benefit brought by noise removal. Actually, as the signal bandwidth is independent of the sampling frequency, so is the used digital filter. It then turns out from Fig. 14 that higher SNR can be achieved using f_s instead of f_{s2} as the noise level within the filter passband is in this case twice lower.

We evaluated the effect of AWGN aliasing by conducting additional measurements at 5 m spatial resolution, reducing this time the sampling frequency f_s from 200 MHz down to
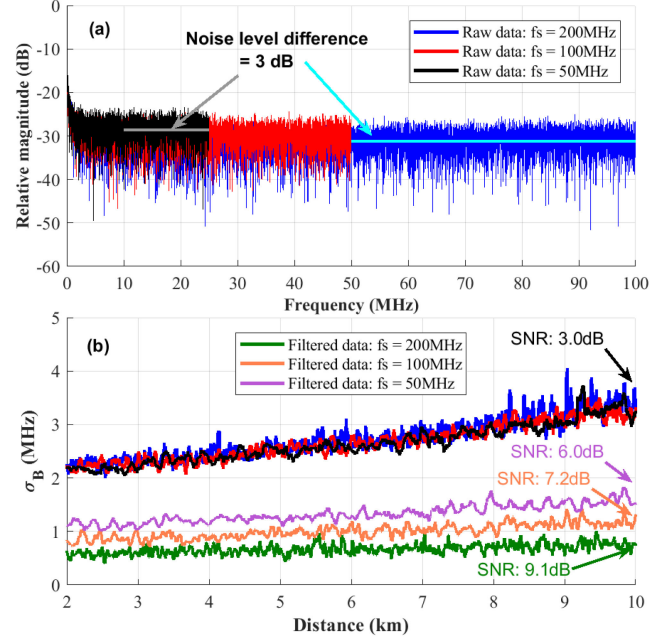

Fig. 15. (a) Relative magnitude of the 2D Fourier transform of the BOTDA matrix along the BGS axis at 5 m SR for $f_s =$ 50 MHz, 100 MHz, and 200 MHz. (b) BFS uncertainty before and after 1D Gaussian filtering (σ_{BGP})

50 MHz. A larger spatial resolution was deliberately set, making it possible to reduce the sampling frequency without aliasing the signal. Fig. 15(a) illustrates a rising of the noise level when the sampling frequency decreases, thus undermining the potential noise reduction, a conclusion corroborated by Fig. 15(b), which displays the BFS uncertainty before and after filtering when changing the sampling frequency. Notice how reducing the sampling frequency by a factor 4, i.e., from 200 MHz to 50 MHz, leads to an SNR increase difference of 3 dB, in agreement with the simple model depicted in Fig. 14 and corroborated by a theoretical analysis conducted in section IV-D3.

3) SNR Improvement and Noise Equivalent Bandwidth: In BOTDA, SNR is usually not computed in terms of ratio between signal and noise power; instead we may use

$$\text{SNR} = \frac{\mu}{\sigma_n} \qquad (3)$$

where μ is the signal mean value and σ_n is the noise standard deviation, both evaluated at the fiber BFS [16]. In estimating the improvement brought by Gaussian filtering, we will assume that the filter does not impact the signal, such that μ is maintained through the filtering operation. SNR improvement results then solely from noise reduction, which is estimated by replacing the Gaussian filter with a perfect rectangular filter with identical noise equivalent bandwidth (NEB), a concept illustrated in Fig. 16. The SNR improvement brought by a 1D Gaussian filter with standard deviation σ_t is given by (see Appendix B for calculation details)

$$\Delta\text{SNR} = \frac{\text{SNR}_{\text{filt}}}{\text{SNR}_{\text{ini}}} = \pi^{\frac{1}{4}}\sqrt{2f_s\sigma_t} \qquad (4)$$
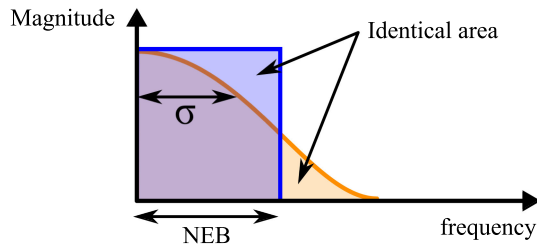
Fig. 16.   Noise equivalent bandwidth (NEB) concept. A filter with a given frequency response is replaced by a perfectly rectangular filter with identical area, such that the filtering of a perfectly white noise leads to identical power rejection.

TABLE II
SNR IMPROVEMENT AFTER 1D GAUSSIAN FILTERING

	Calculated	Measured
$k_{\mathrm{BGP}} = 1$	5.8 dB	4.6 dB
$k_{\mathrm{BGP}} = 2$	4.3 dB	3.9 dB
$k_{\mathrm{BGP}} = 3$	3.4 dB	3.3 dB
$k_{\mathrm{BGS}} = 2$	9.7 dB	7.9 dB
$k_{\mathrm{BGS}} = 4$	8.2 dB	7.6 dB
$k_{\mathrm{BGS}} = 6$	7.4 dB	7.1 dB

The results were calculated using (4), as well as directly measured with an initial SNR of 3.1 dB.

The results obtained using (4) are then compared with the ones provided in section IV-B, which are copied in Table II for convenience. The sampling frequency f_s for the case of the BGP filter corresponds to the actual sampling rate of our acquisition card, i.e., 200 MHz here. For the case of the BGS filter, the sampling frequency corresponds to the inverse of the frequency detuning scanning step (1 MHz), that is 1 μs. The standard deviation σ_t for each filter is given by (2). The results are synthesized in Table II. Overall, the calculated SNR improvements are in good agreement with the measured ones. Notice than when k_{BGP} and k_{BGS} is small, i.e., when the filter is strong, (4) tends to highly overestimate the SNR improvement. This is not surprising, as for such values of k_{BGP} and k_{BGS}, the corresponding filters cutoff frequencies are within the signal bandwidth (see Fig. 10 and 12), and thus the assumption we made in deriving (4) is no longer valid. Finally, we acknowledge that our results could be slightly improved, since our sampling frequency (200 MHz), is not twice greater than our detector bandwidth (125 MHz). Unfortunately, this was the maximum sampling frequency available on our acquisition card.

E. NLM and the ODWT as Low-Pass Filters

In this section, we analyze the operating principles of NLM and the ODWT for noise removal. It turns out that both methods eventually act as low-pass filters, especially at low SNR. Yet, this low-pass filtering is ill-adapted for BOTDA measurements, for which we have a large amount of *a priori* knowledge. This explains why for such a specific case, the proposed Gaussian filter outperforms these two sophisticated techniques.

TABLE III
IMPACT OF VARYING THE THRESHOLD LEVEL IN THE ODWT WHEN USING HARD THRESHOLDING

Threshold level	Details coefficients after thresholding	Result observed
k = 0.25	< 15%	Low improvement
k = 0.5	< 0.5%	Optimal case
k = 1	0 %	Strong smoothing

1) ODWT: Surviving Thresholding: As detailed in Appendix A–C, the orthogonal discrete wavelet transform decomposes a signal using two complementary filters. Such filters partition the signal's energy into low and high frequency components, enabling if wanted a flawless reconstruction. The samples collected at the output of the low-pass filter are an approximation of the original signal, whereas the remaining coefficients withhold information about the signal high frequency content. The essence of noise removal using this algorithm relies on focusing the signal's energy into a reduced set of high value details coefficients, which should capture its features accurately. The low value details coefficients are then assumed to originate from noise, or are considered insignificant to reconstruct the signal, such that they are discarded by thresholding.

The performances of the ODWT were evaluated by inspecting the output SNR, BFS uncertainty and SR impairment over a broad range of parameters. Namely, we managed to change the mother wavelet, that defines the filters' shape, the value of the computed threshold as well as the type of thresholding (soft or hard). The used mother wavelet was found somehow irrelevant in our case, as similar performances could be obtained by empirically adjusting the other parameters to each situation. We focus therefore on the mother employed in the rest of this paper for this explanation, which is the symlet 7.

The key parameter of the ODWT is the level of the thresholding, which could be adjusted in our case by tuning a parameter k (see Appendix A–C for details). The two extreme cases of $k = 0$ and $k \rightarrow \infty$ correspond to letting the signal intact and completely removing any high frequency content, respectively. For intermediate values, a trade-off is expected between noise removal and signal smoothing, as intuitively anticipated. The special case of $k = 1$ corresponds to the universal threshold T_u [29]. Optimal performances were obtained for $k = 0.5$ using hard thresholding, whatever the preset spatial resolution and initial SNR. Table III shows the fraction of detail coefficients that survived the thresholding operation when $k = \{0.25, 0.5, 1\}$, as well as a qualitative description of the obtained results.

The results indicate that in any case, all detail coefficients are within $[-T_u, T_u]$. Setting $k = 1$ thus corresponds to discarding all details coefficients, resulting in a low-pass filtering operation using an ill-adapted filter. Even in the ideal case, most of the coefficients do not exceed the threshold, so that the overall operation is close to a low-pass filtering. Note that the threshold value is independent of the type of thresholding, i.e., hard or soft thresholding, and only the soft case shrinks the remaining
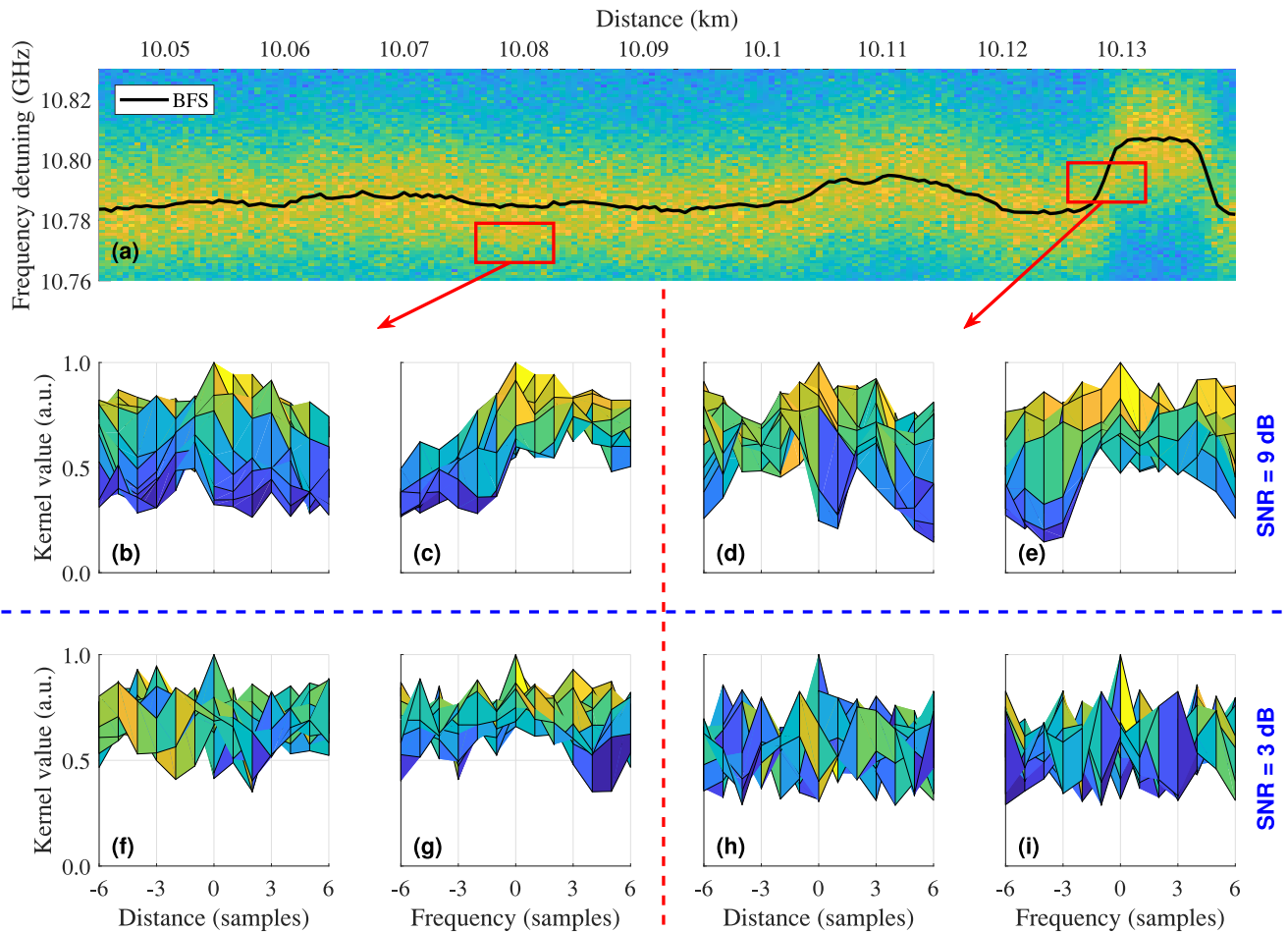
Fig. 17. (a) Heat map indicating the Brillouin gain at fiber end, together with the determined BFS. (b) to (i) kernel $k(i,j)$ (5) computed at two different locations (left and right side of the red dashed line) for two different SNR levels (lower and upper side of the blue dashed line). The x-axis in the figures indicate which side of the kernel is being observed.

coefficients by T_u (wavelet shrinkage). For a fair comparison, the threshold level using soft thresholding should be approximatively half that used for hard thresholding [29]. In our case, we found slightly better results using hard thresholding, although the overall performances are similar.

2) NLM: Similarity and SNR: As detailed in Appendix A–B, NLM performs noise removal by computing at each point a weighted average over the direct neighbors surrounding the processed sample. The size of this kernel is defined by the search window, which was adjusted to 13×13 in our case, and its values are defined by the similarities between two points. The (unnormalized) kernel is given by

$$k(i,j) = \exp\left(-\frac{\|f(P_i) - f(P_j)\|_2^2}{h^2}\right) \quad (5)$$

where $P_{i,j}$ is a 3×3 window centered around i, j and h is a parameter governing the exponential function decay. In our case, h was set to 5 times the white noise standard deviation, which was first estimated using the wavelet decomposition (see Appendix A–C for details). We investigate how NLM behaves by computing the final weighted kernel $k(i,j)$ at two positions and two different SNR levels. The results are shown in Fig. 17.

At high SNR (9 dB), the kernel adapts to the underlying signal, providing more weights to regions with higher similarity. For example, consider Fig. 17(b) and (c) which correspond to a location on the slope of the BGS, in a region where the fiber BFS is quite uniform. On one hand, the Brillouin gain remains approximatively constant with distance, such that the similarity varies little in that direction. On the other hand, the Brillouin gain follows the BGS distribution in the BGS direction, leading to a decrease in similarity. The kernel also adjusts when the BFS varies rapidly, as shown in (d) and (e), where this time both directions present similarity variations. The adaptive behavior of the NLM kernel is however suffering from a poor SNR, as shown in Fig. 17(f) to (i). The noise level makes it impossible for the algorithm to identify regions with higher similarities, such that the adaptive kernel becomes flat, and produces an effect similar to a moving average filter. Note that this filter is stronger when the underlying signal is regular ((f) and (g) compared to (h) and (i)), which might explain why NLM produces such strong smoothing on regions of regular BFS (see Fig. 11). We found no major difference in terms of response when trying to correct this effect by changing either the size of the similarity window or h.

V. CONCLUSION

In this study, we thoroughly analyzed the impact of 2D signal processing on BOTDA measurements. Using the separability property of a 2D Gaussian filter, we clarify the reasons supporting the improvements observed in both signal-to-noise ratio and in uncertainty σ_B on the estimation of the Brillouin frequency shift (BFS). Such gain in performance cannot be made arbitrarily high yet, and must somehow face fundamental limits. For convenience, we here highlight the most important aspects relevant to the post-processing of BOTDA measurements, and provide some guidelines on the potential benefits and limitations of this tool.

1) Any denoising process on the measured spectral distribution of gain at one location (BGS) will bring no decisive improvement in uncertainty σ_B on the BFS estimation, as it is fundamentally redundant with functionally targeted BFS estimation methods, e.g., quadratic fitting. In other words, SNR improvement resulting from noise removal over the BGS will not benefit the experimental uncertainty.

2) BFS uncertainty can be reduced proportionally to the SNR improvement resulting from the processing of each temporal trace at a given frequency, namely the Brillouin gain profile (BGP). However, no BFS uncertainty reduction can be obtained should the analog bandwidth of the acquisition system match that of the measured signal. Under such conditions, the maximum achievable SNR may be readily evaluated [30].

3) Essentially, SNR improvement by post-processing over each BGP results from an *a posteriori* reduction of the system initial analog bandwidth to make it match the signal response, hence suppressing noise lying outside of the signal bandwidth. This may be made optimal by designing and using e.g. a matched filter. For optimal performances, i.e., to achieve highest noise removal, the sampling frequency must be at least twice greater than the bandwidth of the overall acquisition system (i.e., initial analog bandwidth), thus strictly disabling signal or AWGN aliasing.

4) After a careful optimization of the system bandwidth, special care [20] must be given to optimize the method used to estimate the BFS (fitting, cross-correlation, etc.), since the full potential of a given setup would otherwise not be fully exploited, in addition to invalidate any further comparison with other systems or methods.

As a final word, we firmly believe that the aforementioned items draw a theoretical limit to the lowest achievable uncertainty on the BFS estimation for BOTDA distributed systems, since this proper match of the system bandwidth combined to an optimized and targeted BFS extraction method fully take best advantage of all the information content in the BOTDA matrix. We come to the clear conclusion that any processing – even extremely sophisticated, such as image processing, deep learning, etc., – brings no tangible benefit on a configuration optimized in terms of detection bandwidth and fitting procedure. Such a processing can be helpful to correct imperfections in the design and sometimes screen poor intrinsic performance.

Nevertheless, we keep convinced that a proper and well thought experimental design must be the preferred avenue to reach the best performance.

APPENDIX A
IMAGE PROCESSING TECHNIQUES

A. Separable 2D Gaussian Filter

A 1D Gaussian filter $g_{1D}(x_i)$ is solely defined on a given axis x_i by its standard deviation σ_i as:

$$g_{1D}(x_i) = \frac{1}{\sqrt{2\pi}\sigma_i} e^{-\frac{x_i^2}{2\sigma_i^2}} \tag{6}$$

A 2D separable Gaussian filter $g_{2D}(x_1, x_2)$ is built upon this definition by simple multiplication:

$$g_{2D}(x_1, x_2) = g_{1D}(x_1)g_{1D}(x_2) \tag{7}$$

2D filtering using a separable filter is thus equivalent to the successive application of the separate one dimensional filters on the rows and column of a 2D matrix. The filtering operation may be conducted either in time domain using a convolution, or in the frequency domain by Fourier transform multiplication.

B. Non-Local Means

Low-pass filters lie among the simplest methods employed for noise removal in images. They replace the value of each pixel by a weighted average of the surrounding pixels, based on the assumption that the underlying signal shows some continuity. This explains why low-pass filters may smoothen sharp transitions, resulting in the blurring of some contours in images. The non-local means (NLM) algorithm [24] is based on the observation that pixels sharing a similar value might not necessarily lie in close vicinity. It associates to the pixel i a weight $w(i, j)$:

$$w(i, j) = \frac{1}{Z(i)} \exp\left(-\frac{||f(P_i) - f(P_j)||_2^2}{h^2}\right) \tag{8}$$

where $Z(i)$ is a normalization factor given by

$$Z(i) = \sum_j \exp\left(-\frac{||f(P_i) - f(P_j)||_2^2}{h^2}\right) \tag{9}$$

Here $f(P_{i,j})$ designates the value taken by the image over square patches centered around pixel i or j respectively while h is a parameter controlling the exponential decay and consequently the filtering strength. The NLM algorithm thus compares the similarity between patches based on their Euclidean distance. Practically, the searching range S is limited to a given region around the considered pixel as the algorithm would otherwise require excessive computation times. Based on the similarity search performed in (8), each pixel $f(i)$ is replaced by:

$$f(i) = \sum_{\forall j \in S} w(i, j)f(j) \tag{10}$$

C. The Discrete Wavelet Transform

Wavelets designate a specific class of zero-average functions that found countless applications in signal processing, notably
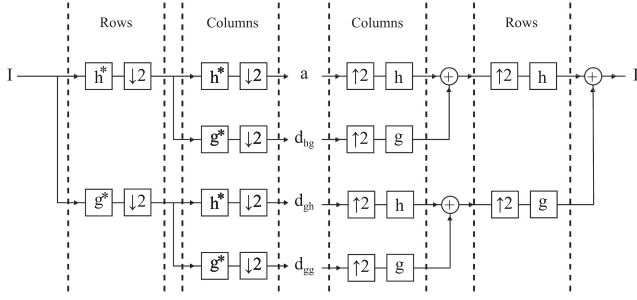
Fig. 18. 2D signal decomposition and perfect reconstruction based on the orthogonal discrete wavelet transform (ODWT). Here $h^*[n] = h[-n]$ and $g^*[n] = g[n]$.

for image compression. Although the scope covered by wavelets is extremely broad, we shall restrict their application to noise removal in images using the so called orthogonal discrete wavelet transform (ODWT). It relies on a multiscale decomposition of the image I thanks to the use of tightly related filters denoted h and g as illustrated in Fig. 18.

These filters build a perfect reconstruction filter bank, since they enable to recover the original image I without information loss. Note that such filter banks have originally no connection with wavelets; rather it was found that wavelets based filters enable to build such banks. The filters h and g make a unit partition of the signal spectrum. In other terms, h is a low-pass filter such that its output a (for approximation coefficients) is a low-pass version of the original signal whereas g is a high-pass filter which output d (for detail coefficients) contains the signal high-frequency information. 2D signals such as images are decomposed in four distinct regions: the low-pass approximation of the original image (a), the vertical details (d_{hg}), the horizontal details (d_{gh}) and the diagonal details (d_{gg}). The decomposition can be carried further at coarser scales on a, leading to a multiscale representation of the original image. The ODWT relies on the concept that most of the details coefficients d will be of low magnitude, except for regions where I exhibits rapid variations. Noise removal is achieved by assuming that details coefficients which value fall below a certain threshold carry no valuable information and can be discarded before reconstructing I. The threshold T_u used in this paper is called the universal threshold and is defined as:

$$T_u = k\sigma_n \sqrt{2\log(N)} \qquad (11)$$

Here σ_n is the noise standard deviation and N is the number of samples in the image. The parameter k does not appear in the original definition but was introduced to finely adjust the threshold value. A remarkable feature of the wavelet transform is that it enables estimating the noise level based on the details coefficients d_{gg} computed at the finest scale:

$$\hat{\sigma}_n = \frac{\text{median}(d_{gg})}{0.6745} \qquad (12)$$

After estimation of the threshold level, thresholding is applied on the detail coefficients d only following a hard or soft

thresholding operation:

$$\text{Hard threshold:} \quad d_H = d \cdot \{|d| > T_u\} \qquad (13)$$

$$\text{Soft threshold:} \quad d_S = \text{sgn} \cdot \max(|x| - T_u, 0) \qquad (14)$$

Hard thresholding discards coefficients which magnitude is smaller than T_u and preserve the others while soft thresholding also reduces the magnitude of the remaining coefficients by T_u.

APPENDIX B
NOISE EQUIVALENT BANDWIDTH

We provide here the expression of the Fourier transform in terms of frequency for a temporal Gaussian signal denoted $g(t)$ and defined as

$$g(t) = \frac{1}{\sqrt{2\pi}\sigma_t} e^{-\frac{t^2}{2\sigma_t^2}} \qquad (15)$$

where σ_t is the standard deviation of the Gaussian function and $g(t)$ is assumed to be centered at $t = 0$. This assumption has no consequence on the final result and slightly simplifies the calculation. The Fourier transform $\hat{g}(f)$ of $g(t)$ is given by

$$\hat{g}(f) = \int_{-\infty}^{\infty} g(t)e^{-i2\pi ft}dt = e^{-2\pi^2\sigma_t^2 f^2} \qquad (16)$$

which enables to calculate the noise equivalent bandwidth (NEB)

$$\text{NEB} = \int_0^{\infty} |\hat{g}(f)|^2 \, df = \frac{1}{\sqrt{\pi}4\sigma_t} \qquad (17)$$

where a one-sided spectrum is considered. For a constant noise power spectral density N_0 spanning over a bandwidth NEB, the noise variance σ_{filt}^2 is by definition

$$\sigma_{\text{filt}}^2 = 2N_0\text{NEB} \qquad (18)$$

where we considered integration over a double sided spectrum. The initial noise variance is given by

$$\sigma_n^2 = N_0 f_s \qquad (19)$$

such that the SNR improvement obtained following the definition (3) and assuming $\mu = $ constant is given by

$$\Delta\text{SNR} = \frac{\text{SNR}_{\text{filt}}}{\text{SNR}_{\text{ini}}} = \sqrt{\frac{\sigma_n^2}{\sigma_{\text{filt}}^2}} = \pi^{\frac{1}{4}}\sqrt{2f_s\sigma_t} \qquad (20)$$

REFERENCES

[1] R. W. Boyd, *Nonlinear Optics*. San Diego, CA, USA: Academic Press, 2008.

[2] G. P. Agrawal, *Nonlinear Fiber Optics*. San Diego, CA, USA: Academic Press, 2007.

[3] T. Horiguchi, T. Kurashima, and M. Tateda, "A technique to measure distributed strain in optical fibers," *IEEE Photon. Technol. Lett.*, vol. 2, no. 5, pp. 352–354, May 1990.

[4] T. Kurashima, T. Horiguchi, and M. Tateda, "Distributed-temperature sensing using stimulated brillouin scattering in optical silica fibers," *Opt. Lett.*, vol. 15, no. 18, pp. 1038–1040, Sep. 1990. [Online]. Available: http://ol.osa.org/abstract.cfm?URI=ol-15-18-1038

[5] M. Alem, M. A. Soto, and L. Thévenaz, "Analytical model and experimental verification of the critical power for modulation instability in optical fibers," *Opt. Express*, vol. 23, no. 23, pp. 29 514–29 532, Nov. 2015. [Online]. Available: http://www.opticsexpress.org/abstract.cfm?URI=oe-23-23-29514

[6] A. Minardo, R. Bernini, and L. Zeni, "A simple technique for reducing pump depletion in long-range distributed brillouin fiber sensors," *IEEE Sensors J.*, vol. 9, no. 6, pp. 633–634, Jun. 2009.

[7] L. Thévenaz, S. F. Mafang, and J. Lin, "Effect of pulse depletion in a brillouin optical time-domain analysis system," *Opt. Express*, vol. 21, no. 12, pp. 14 017–14 035, Jun. 2013. [Online]. Available: http://www.opticsexpress.org/abstract.cfm?URI=oe-21-12-14017

[8] A. Dominguez-Lopez, X. Angulo-Vinuesa, A. Lopez-Gil, S. Martin-Lopez, and M. Gonzalez-Herraez, "Non-local effects in dual-probe-sideband brillouin optical time domain analysis," *Opt. Express*, vol. 23, no. 8, pp. 10 341–10 352, Apr. 2015. [Online]. Available: http://www.opticsexpress.org/abstract.cfm?URI=oe-23-8-10341

[9] A. Dominguez-Lopez *et al.*, "Novel scanning method for distortion-free botda measurements," *Opt. Express*, vol. 24, no. 10, pp. 10 188–10 204, May 2016. [Online]. Available: http://www.opticsexpress.org/abstract.cfm?URI=oe-24-10-10188

[10] F. Rodriguez-Barrios *et al.*, "Distributed brillouin fiber sensor assisted by first-order raman amplification," *J. Lightw. Technol.*, vol. 28, no. 15, pp. 2162–2172, Aug. 2010.

[11] M. A. Soto, G. Bolognini, F. D. Pasquale, and L. Thévenaz, "Long-range brillouin optical time-domain analysis sensor employing pulse coding techniques," *Meas. Sci. Technol.*, vol. 21, no. 9, Jul. 2010, Art. no. 094024.

[12] S. L. Floch, F. Sauser, M. Llera, and E. Rochat, "Novel brillouin optical time-domain analyzer for extreme sensing range using high-power flat frequency-coded pump pulses," *J. Lightw. Technol.*, vol. 33, no. 12, pp. 2623–2627, Jun. 2015.

[13] Z. Yang, M. A. Soto, and L. Thévenaz, "Increasing robustness of bipolar pulse coding in brillouin distributed fiber sensors," *Opt. Express*, vol. 24, no. 1, pp. 586–597, Jan. 2016. [Online]. Available: http://www.opticsexpress.org/abstract.cfm?URI=oe-24-1-586

[14] Z. Yang, Z. Li, S. Zaslawski, L. Thévenaz, and M. A. Soto, "Design rules for optimizing unipolar coded brillouin optical time-domain analyzers," *Opt. Express*, vol. 26, no. 13, pp. 16 505–16 523, Jun. 2018. [Online]. Available: http://www.opticsexpress.org/abstract.cfm?URI=oe-26-13-16505

[15] M. A. Soto, J. A. Ramírez, and T. Luc, "Intensifying the response of distributed optical fibre sensors using 2d and 3d image restoration," *Nature Commun.*, vol. 7, 2016. [Online]. Available: https://www.nature.com/articles/ncomms10870

[16] M. A. Soto and L. Thévenaz, "Modeling and evaluating the performance of brillouin distributed optical fiber sensors," *Opt. Express*, vol. 21, no. 25, pp. 31 347–31 366, Dec. 2013. [Online]. Available: http://www.opticsexpress.org/abstract.cfm?URI=oe-21-25-31347

[17] M. Alem, M. A. Soto, M. Tur, and L. Thévenaz, "Analytical expression and experimental validation of the brillouin gain spectral broadening at any sensing spatial resolution," vol. 10323, 2017. [Online]. Available: https://doi.org/10.1117/12.2267639

[18] A. W. Brown, M. DeMerchant, X. Bao, and T. W. Bremner, "Spatial resolution enhancement of a brillouin-distributed sensor using a novel signal processing method," *J. Lightw. Technol.*, vol. 17, no. 7, pp. 1179–1183, Jul. 1999.

[19] M. A. Farahani, E. Castillo-Guerra, and B. G. Colpitts, "Accurate estimation of brillouin frequency shift in brillouin optical time domain analysis sensors using cross correlation," *Opt. Lett.*, vol. 36, no. 21, pp. 4275–4277, Nov. 2011. [Online]. Available: http://ol.osa.org/abstract.cfm?URI=ol-36-21-4275

[20] S. M. Haneef, Z. Yang, L. Thévenaz, D. Venkitesh, and B. Srinivasan, "Performance analysis of frequency shift estimation techniques in brillouin distributed fiber sensors," *Opt. Express*, vol. 26, no. 11, pp. 14 661–14 677, May 2018. [Online]. Available: http://www.opticsexpress.org/abstract.cfm?URI=oe-26-11-14661

[21] H. Wu, L. Wang, Z. Zhao, N. Guo, C. Shu, and C. Lu, "Brillouin optical time domain analyzer sensors assisted by advanced image denoising techniques," *Opt. Express*, vol. 26, no. 5, pp. 5126–5139, Mar. 2018. [Online]. Available: http://www.opticsexpress.org/abstract.cfm?URI=oe-26-5-5126

[22] S. Zaslawski, Z. Yang, M. A. Soto, and L. Thévenaz, "Impact of fitting and digital filtering on signal-to-noise ratio and brillouin frequency shift uncertainty of botda measurements," in *Proc. 26th Int. Conf. Opt. Fiber Sensors*, 2018, Art. no. ThE27. [Online]. Available: http://www.osapublishing.org/abstract.cfm?URI=OFS-2018-ThE27

[23] S. G. Mallat, "A theory for multiresolution signal decomposition: the wavelet representation," *IEEE Trans. Pattern Anal. Mach. Intell.*, vol. 11, no. 7, pp. 674–693, Jul. 1989.

[24] A. Buades, B. Coll, and J. Morel, "A non-local algorithm for image denoising," in *Proc. IEEE Comput. Soc. Conf. Comput. Vision Pattern Recognit.*, Jun. 2005, vol. 2, pp. 60–65 vol. 2.

[25] S. L. Floch and F. Sauser, "New improvements for brillouin optical time-domain reflectometry," in *Proc. 25th Opt. Fiber Sensors Conf.*, Apr. 2017, pp. 1–4.

[26] R. W. Schafer, "What is a savitzky-golay filter? [lecture notes]," *IEEE Signal Process. Mag.*, vol. 28, no. 4, pp. 111–117, Jul. 2011.

[27] E. A. Lee and D. G. Messerschmitt, *Digital Communication, Second Edition*. Norwell, MA, USA: Kluwer Academic Publishers, 1994.

[28] C. A. Gobet, "Spectral distribution of a sampled 1st-order lowpass filtered white noise," *Electron. Lett.*, vol. 17, no. 19, pp. 720–721, Sep. 1981.

[29] S. G. Mallat, *A Wavelet Tour of Signal Processing, 3rd Edition*. San Diego, CA, USA: Academic Press, 2008.

[30] S. Wang, Z. Yang, M. A. Soto, and L. Thévenaz, "Optimizing the signal-to-noise ratio for direct-detection BOTDA," in *Proc. 7th Eur. Workshop Opt. Fibre Sensors*, SPIE, 2019, vol. 11199, pp. 359–362. [Online]. Available: https://doi.org/10.1117/12.2540930

Simon Zaslawski received the M.Sc. degree in electrical engineering from the Swiss Federal Institute of Technology of Lausanne, Lausanne, Switzerland, in 2015, where he is currently working toward the Ph.D. degree in photonics. His research interest includes distributed optical fiber sensors, optoacoustic effect, and signal processing.

Zhisheng Yang (Member, OSA) received the B.E. degree in optoelectronics from the Beijing Institute of Technology, Beijing, China, in 2010, and the Ph.D. degree in communication and information system from the Beijing University of Posts and Telecommunications, Beijing, in 2016. His Ph.D. research work, performed with the Institute of Information Photonics and Optical Communications, was focused on distributed optical fiber sensors.

In 2016, he joined the Group for Fibre Optics, Swiss Federal Institute of Technology of Lausanne, Switzerland, as a Postdoctoral Researcher. His main research interests include optical fiber sensing, nonlinearities in optical fiber.

Dr. Yang is a Member of the Optical Society (OSA).

Luc Thévenaz (Fellow, OSA) received the M.Sc. and Ph.D. degrees in physics from the University of Geneva, Geneva, Switzerland, in 1982 and 1988, respectively.

In 1988, he joined the Swiss Federal Institute of Technology of Lausanne, Lausanne, Switzerland, where he currently leads a research group involved in photonics, namely fiber optics and optical sensing. Research topics include Brillouin-scattering fiber sensors, slow and fast light, nonlinear fiber optics, and laser spectroscopy in gases. He achieved with his collaborators the first experimental demonstration of optically controlled slow and fast light in optical fibers, realized at ambient temperature and operating at any wavelength since based on stimulated Brillouin scattering. He also contributed to the development of Brillouin distributed fiber sensing by proposing innovative concepts pushing beyond barriers. During his career, he stayed with Stanford University, Korea Advanced Institute of Science and Technology, Tel Aviv University, University of Sydney, Polytechnic University of Valencia. In 2000, he cofounded the company Omnisens that is developing and commercializing advanced photonic instrumentation based on distributed fiber sensing.

Prof. Thévenaz is the co-Executive Editor-in-Chief for the journal *Nature Light: Science & Applications* and is a Member of the Editorial Board (Associate Editor) for the journal *APL Photonics & Laser & Photonics Reviews*. He is also a Fellow of Optical Society (OSA).